Journal of Materials Chemistry C

ROYAL SOCIETY OF CHEMISTRY

PAPER

Published on 29 June 2026
Licence and permissions

Check for updates

Cite this: DOI: 10.1039/d6tc01261b

van der Waals engineering of the valley polarization in WSe_2 *via* the Kagome V_2O_3 monolayer heterostructure through magnetic proximity effect

Fazle Subhan, [a] Kiduk Kim, [a] Jaeyoung Kim, [a] Guangzhao Qin,*[b] Luqman Ali[c] and Joonkyung Jang *[a]

Achieving a robust valley splitting in transition metal dichalcogenides (TMDs) at zero magnetic field is challenging and elusive for valleytronic and spintronic devices. Therefore, in the current study, using first principles calculations, we introduce an oxide-driven valleytronic platform by employing a two-dimensional ferromagnetic oxide (V_2O_3) as a magnetic proximity partner for WSe_2. We found that the intrinsic ferromagnetism of V_2O_3 induces a prominent and spontaneous valley splitting of ~10.41 meV in WSe_2. This pronounced valley polarization mainly originates from strong interfacial exchange coupling interactions and charge redistribution mediated by V 3d electrons, coupled with the intrinsic spin–orbit coupling of WSe_2. Interestingly, this value is significantly greater than the previously reported value for CrI_3/WSe_2, which corresponds to an effective magnetic field of ~10 T. Besides, we also determined a high Curie temperature of 500 K and an out-of-plane magnetic anisotropy energy (MAE) of 0.31 meV, indicating that this oxide-based heterostructure can also be used in near-room temperature operation. Importantly, under an external electric field with a step of ±0.1 eV $Å^{-1}$, the ferromagnetism is still preserved and an enhancement in the Curie temperature and MAE makes this oxide-based heterostructure more valuable for next-generation valleytronic devices. Therefore, these findings establish a new paradigm for realizing tunable, robust, and magnetic field-free valleytronic and spintronic devices using this oxide-based heterostructure. Moreover, this concept can be generalized to other correlated oxide-based TMDs systems, providing a versatile strategy for next-generation quantum and functional materials.

Received 21st April 2026,
Accepted 27th June 2026

DOI: 10.1039/d6tc01261b

rsc.li/materials-c

I. Introduction

The family of two-dimensional (2D) materials has grown enormously, unlocking new paradigms and accelerating the investigation of potential phenomena with rich physics. The emergence of two-dimensional magnetic materials, such as CrI_3,[1] VI_3,[2] $Cr_2Ge_2Te_6$[3] and Fe_3GeTe_2,[4] up to the low-dimensionality, has also triggered researchers to explore new insights using van der Waals (vdW) heterostructures. These possible new 2D materials and their vdW heterostructures have exponentially increased the huge expansion of different materials in condensed matter physics over the last few years. Interestingly, the band alignment in these vdW heterostructures provides many ideal platforms and enables new developments, such as the manipulation of spintronic,[5] excitonic,[6] topological[7] and superconducting[8] phenomena. Apart from the individual materials in 2D monolayers, stacking in different forms can also help to achieve improved functions.[9] The valley polarization can be controlled in YI_2, LaI_2 and $GdBr_2$ in their 2D van der Waals bilayers.[10] Furthermore, some of the well-established theories, such as the Berezinskii–Kosterlitz–Thouless (BKT) transition of the XY model,[11,12] Mermin–Wagner theorem[13] and Ising transition,[14] also provide a way to thoroughly study the magnetic vdW heterostructures. Interestingly, modern semiconductor heterostructures play a vital role in industries and technologies due to their prominent properties in electronics, opto-electronics and valleytronics devices.[15] However, no enthusiastic efforts have been made in the past for exfoliating and potentially using them as a substrate in the individual monolayer, except for the theoretical efforts.

In graphene-like 2D materials, owing to the quantum Hall effects[16] and the breaking of time reversal symmetry, the two inequivalent corners of the Brillouin zone (±K) give rise to another prominent phenomenon called valley pseudospins.

[a] Department of Nanofusion Technology, Pusan National University, Busan 46241, Republic of Korea. E-mail: jkjang@pusan.ac.kr
[b] State Key Laboratory of Advanced Design and Manufacturing Technology for Vehicle, College of Mechanical and Vehicle Engineering, Hunan University, Changsha 410082, P. R. China. E-mail: gzqin@hnu.edu.cn
[c] Department of Physics, University of Virginia, Charlottesville, VA, 22911, USA

Since valleys emerge at the corners of the hexagonal Brillouin zone as two degenerated states, they offer significant potential for device applications.[17,18] Experimentally, circularly polarized optical pumping is employed to selectively excite valley pseudospins, while a high magnetic field induces Zeeman splitting, which leads to the breaking of time-reversal symmetries. Furthermore, the optical Stark effect provides an alternative way to lift the valley degeneracy by inducing an effective large magnetic field, even in the absence of an external magnetic field. Interestingly, the presence of valley degeneracy in the momentum space of transition metal dichalcogenides (TMDs) leads to a variety of emerging physical phenomena, such as valleytronics,[19–21] valley Hall effects[22] and valley-dependent photoluminescence.[23] In 2D materials, the time-reversal symmetry enforces energetic degeneracy and couples the two inequivalent valleys; therefore, its breaking can profoundly alter the electronic properties.[24] Interestingly, Mak *et al.* experimentally demonstrated the valley Hall effect in a MoS_2 monolayer, where carriers originate from different valleys with a propagation in the opposite transverse directions.[25] Mostly, due to the strong spin–orbit coupling (SOC) effect in the Group VI TMDs and the breaking of time-reversal symmetry, the valleytronics and Rashba effect occurred. Besides different approaches such as stacking effect,[26] twisting and gate voltage,[27] external magnetic field,[28] creating vacancies,[29] and doping with magnetic ions,[30] strain,[31] and layer engineering approaches[32,33] in the vdW heterostructure can also be used to achieve valley splitting. Similarly, doping in the Fe_2Se_2O monolayer and a perpendicular Néel vector in colinear anti-ferromagnetic materials, such as Co_2S_2, can lead to multifunctional spintronic and valleytronic devices.[34,35] Further, the layer polarized spin Hall effect (LP-SHE) in bilayers can also make a 2D material an ideal candidate for spintronic applications.[36] Among all these approaches, the van der Waals effect for inducing valley splitting[37] and the magnetic proximity effect in the vdW heterostructure are very prominent.[27,38]

Moreover, 2D van der Waals materials can not only widen and enhance valley studies but when engineered with a TMD 2D material can also broaden spin-dependent charge hopping across the interface of the vdW heterostructure by the excitation helicity-dependent photoluminescence intensity.[39] Interestingly, some researchers also confirmed the dependency of valley splitting on the interlayer distance,[26,40] while others have reported on the interlayer twisting.[41] Besides, Zhang *et al.* and Imran *et al.* investigated the stacking-dependent approach for lifting the valleys in heterostructures.[26,42] These studies clearly prove that valley manipulation in TMDs can be easily achieved from a ferromagnetic substrate, which causes a proximity effect. This proximity effect is a straightforward and promising approach for valley polarization.

The heterostructures have received a prominent resurgence of interest in 2D magnetic materials to fabricate heterostructures comprising TMD and ferromagnetic monolayers and to overcome challenges for applications in electronics, valleytronics and spintronics. However, the oxide materials, or more specifically vanadium oxide, still need to be explored both experimentally and theoretically. Therefore, in our current study, we performed first principles calculations of valley splitting in a WSe_2 monolayer on a 2D magnetic oxide substrate, the V_2O_3 monolayer, and additionally explored the magnetic proximity effect. Because both electrons and holes do not have an equal space extremum at K^+ and K^- but instead have degenerate momentum space extremum at K^+ and K^-. Thus, the central issue in the current study is enhanced valley splitting and the giant magnetic anisotropy induced by a perpendicular electric field.

II. Numerical method

In the present study, we used density functional theory calculations with the projected augmented wave (PAW) method within the Vienna *ab initio* simulation package (VASP),[43,44] with the generalized gradient approximation (GGA) adopted with the Perdew–Burke–Ernzerhof (PBE) functional.[45] For the plane wave kinetic energy cut-off of 500 eV was used. The Brillouin zone has been sampled by the Monkhorst–Pack method[46] within an atomically generated *k*-mesh of 11 × 11 × 1. The structural optimization of the V_2O_3/WSe_2 heterostructure was carried out using the DFT-D3 van der Waals correction, and the optimized geometry was subsequently used for all electronic, magnetic, and structural analyses.[47] The convergence criterion for energy was set to 10^{-5} eV, while the atomic positions were optimized until the Hellmann–Feynman force on each atom became smaller than 0.01 eV $Å^{-1}$. To describe the strong correlation effects of the localized V 3d electrons in V_2O_3, the DFT+*U* method was employed. The on-site Coulomb interaction was treated using the Dudarev approach, where only the effective Hubbard parameter $U_{eff} = U - J$ is considered. In the present calculations, U_{eff} = 3.68 eV was applied to the V 3d orbitals.[48,49] For magnetic anisotropy energy (MAE), a non-collinear total energy calculation with spin–orbit coupling (SOC) was adopted for determining the magnetization direction. The energy criterion was set to 10^{-8} and a denser *k*-mesh of 21 × 21 × 1 was used with and without an external electric field. The convergence of magnetic anisotropy energy was carefully checked along the two magnetic axes [100] and [001], which are called parallel (in-plane) and perpendicular (out-of-plane). The energy difference between these two directions (E_{in}–E_{out}) gives us the magnetic crystalline anisotropy energy (MAE). To avoid artificial interactions between the images, a vacuum of more than 20 Å along the *z*-axis was applied. Further, to obtain the Curie temperature (T_C), we calculated the temperature dependent magnetization curve based on the Metropolis Monte Carlo (MC) simulations using the VAMPIRE software package.

III. Results

A. Crystal structure of monolayers

In the current study, as depicted in Fig. 1(a and b), in the V_2O_3 monolayer (ML), where vanadium(v) atoms are surrounded by three O atoms in a hexagonal form, these O atoms also form a honeycomb Kagome lattice structure. The lattice constant of the V_2O_3 ML is 6.193 Å, where the slight reduction in the lattice constant of the V_2O_3 ML after structural relaxation is because of the difference in their atomic radii. Interestingly, the V-to-V

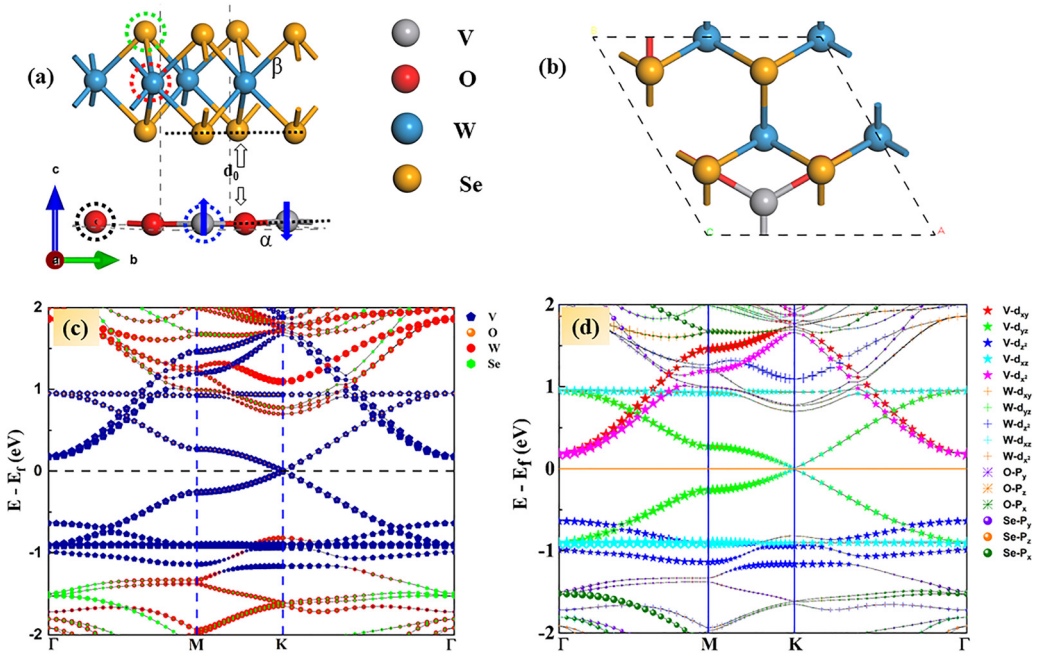

Fig. 1 Structural schematic of the V_2O_3/WSe_2 vdW heterostructures from their (a) side and (b) top views, respectively. The gray, red, sky blue, and orange balls show the V, O, W and Se atoms, respectively. GGA+*U* electronic band structures of the V_2O_3/WSe_2 vdW heterostructure for the (c) majority spin and (d) orbital-resolved in majority spin alignment.

atom distance is 3.576 Å, and similarly, the O–O distance is 3.098 Å. Further, the relaxed crystal structure of the V_2O_3 ML belongs to the space group *P*6/*MMM* (D6H-1) with # 191. We have already reported the formation and binding energies of V_2O_3 ML in our previous report.[49] Besides the formation and binding energies, we also checked the stability of V_2O_3 ML using the phonon and thermodynamic stability in our previous study.[49] Similarly, the hexagonal transition metal dichalcogenide WSe_2 has also been reported. WSe_2 exists in two phases called trigonal (1T) and hexagonal (2H) under normal conditions of temperature and pressure.[50] The 2H phase is energetically more stable; therefore, we consider the 2H phase in our calculations. After full structural optimization, our relaxed lattice constant (3.32 Å) for the WSe_2 monolayer agrees well with the experimentally reported values.[51] The top and side view for the WSe_2 monolayer is given in the Fig. S1(a) and (b), respectively.

B. V_2O_3/WSe_2 heterostructure

Now, to construct the van der Waals (vdW) V_2O_3/WSe_2 heterostructure, the optimized lattice constants of the isolated V_2O_3 and WSe_2 monolayers (MLs) were 6.193 Å and 3.321 Å, respectively. To reduce the lattice mismatch between the two layers, a $1 \times 1 \times 1$ unit cell of V_2O_3 and a $2 \times 2 \times 1$ supercell of WSe_2 (6.642 Å) were employed to build the heterostructure. The lattice mismatch between the two monolayers can be calculated by using the relation below:

$$\delta = (a^{H} - a^{M})/a^{M} \times 100\%, \quad (1)$$

where a^{H} and a^{M} denote the lattice constants of the V_2O_3/WSe_2 heterostructure and V_2O_3 (or WSe_2) MLs, respectively. Based on this relation, the lattice mismatch between V_2O_3 and the $2 \times 2 \times 1$ WSe_2 supercell is approximately 6.87%. To form a commensurate interface, a common in-plane lattice constant of 6.45 Å was adopted. Consequently, the WSe_2 layer undergoes a compressive strain of −2.89% as its lattice constant decreases from 6.642 Å to 6.45 Å, while the V_2O_3 monolayer experiences a tensile strain of about 4.15%, expanding from 6.193 Å to 6.45 Å. The presence of such strain can significantly influence the interlayer coupling and orbital hybridization at the interface, thereby influencing the electronic and structural properties of the V_2O_3/WSe_2 heterostructure. Particularly, previous studies show that compressive strain leads to a notable reduction in the band gap of WSe_2, reaching values of approximately 1.457 eV at around 3% strain.[52] Furthermore, strain-induced modifications in crystal field symmetry and orbital overlap can also change the spin–orbit coupling (SOC) at the interface and thus lead to an effective change in the magnetic anisotropy energy (MAE), while the applied strain can also indirectly alter the thermal stability of the magnetic ordering in V_2O_3/WSe_2 heterostructure. Nevertheless, the dominant mechanism responsible for the observed valley splitting is attributed to the magnetic proximity effect rather than strain alone.[53,54]

To determine the most stable configuration of the V_2O_3/WSe_2 heterostructure, we consider several possible stackings as shown in Fig. S2. The relative stability of each configuration can be easily evaluated from the total energy calculations. To compare the ground state energies of different stackings, the energy of the S1 configuration was taken as the reference (0 meV). The calculated energy differences for the S2, S3 and S4 configurations are 24.48, 76.26 and 77.34 meV, respectively, relative to S1. In contrast to the WSe_2 monolayer, both in the V_2O_3 monolayer and the V_2O_3/WSe_2 heterostructure, we included van der Waals (vdW)

interactions. We also calculated the interlayer distance between V–W and V–Se for different stackings before and after relaxation. The calculated values for the interlayer distance are shown in Fig. S3(a) and (b). Consequently, we discovered that O on top of W, also known as S1 stacking, is the most advantageous of the other stackings in terms of both energies and interlayer distance.

Therefore, the S1 configuration was further investigated for electronic, magnetic, and interfacial properties of the V_2O_3/WSe_2 heterostructure. Besides, we also determined the bond lengths between O–V (α) and W–Se (β) before (after) relaxation to be 1.88 (1.867 Å) and 2.54 (2.537 Å), respectively, which shows no prominent change, while the interlayer distance d_0 before (after) the structural optimization is 2.256 (3.138 Å) in the S1 stacking, as shown in Fig. 1(a) and (b) for top and side views, respectively.

We also calculated the interlayer binding energy using the relation below:

$$E_b = E_{tot} - E_{WSe_2} - E_{V_2O_3}, \quad (2)$$

where E_b is the binding energy and E_{tot} is the total energy of the V_2O_3/WSe_2 heterostructure and E_{WSe_2} and $E_{V_2O_3}$ are the energies of each monolayer, respectively. The total energy of the heterostructure, WSe_2 and V_2O_3, respectively, is $E_{tot} = -128$, $E_{WSe_2} = -86.4$ and $E_{V_2O_3} = -41.1$ eV, which results in a binding energy of $E_b = -133.58$ meV. As we have a total of 17 atoms in the unit cell of the V_2O_3/WSe_2 heterostructure, the binding energy per atom becomes −7.86 meV, which is in accordance with DFT-calculated values for different vdW heterostructures.[26,42] Finally, we apply a perpendicular external electric field in a step of 0.1 V Å^{-1} to the V_2O_3/WSe_2 vdW heterostructure. The electric field is applied in two opposite directions called out-of-plane or positive (from WSe_2 towards V_2O_3 ML) and in-plane or negative (from V_2O_3 towards WSe_2 ML). In the literature, a high impact of the electric field on the electronic and magnetic properties of the 2D V_2O_3/WSe_2 heterostructure has been reported.[42,55] The calculated results for the interlayer distance are given in Table 1.

Table 1 Lattice constants (a), interlayer distances (d_0), total energy differences (ΔE), band gap energies (E_g), energy differences at K^+ and K^- (Δ), and magnetocrystalline anisotropy energies (MAE) for positive/negative electric fields

	Pristine	0.1	0.2	0.3	0.4	0.5	0.6
	Positive						
E_0 (meV)	314.88	341.17	312.64	311.76	310.68	309.6	348.3
d_0 (Å)	3.19	3.148	3.143	3.139	3.135	3.131	3.127
E_g (eV)	0.030	0.019	0.029	0.029	0.032	0.033	0.032
Δ (meV)	10.41	11.18	12.95	15.91	18.50	27.12	38.14
MAE (meV)	0.31	0.37	0.41	0.41	0.42	0.42	0.42
	Negative						
E_0 (meV)	314.88	341.17	312.64	311.76	310.68	309.6	348.3
d_0 (Å)	3.19	3.156	3.199	3.201	3.161	3.244	3.275
E_g (eV)	0.030	0.031	0.029	0.030	0.031	0.032	0.030
Δ (meV)	10.41	10.06	9.51	11.83	14.23	16.84	23.45
MAE (meV)	0.31	0.39	0.38	0.37	0.36	0.36	0.34

C. Electronic properties

The central aim of our current calculations is to investigate valley splitting due to the magnetic proximity effect of the V_2O_3 ML. Therefore, we first need to explore the electronic properties of the V_2O_3/WSe_2 vdW heterostructure using the GGA+U technique. For this purpose, we investigated the spin- and orbital-resolved band structure, as shown in Fig. 1(c) and (d), respectively. Interestingly, Fig. 1(c) and (d) depicts a direct band gap of 0.03 eV for the V_2O_3/WSe_2 vdW heterostructure with a Dirac point on the high-symmetry K point, where both the CBM and VBM are located at the K point. Further, from the spin-resolved projected band structure of the V_2O_3/WSe_2 vdW heterostructure, we observed that only the majority spin of the V atom is responsible for the Dirac point, while all other atoms make negligible contributions, as shown in Fig. 1(c). Further, orbital-resolved band analysis also confirms that the Dirac point mainly originated from the majority spin of the V-d_{yz} orbital, as shown in Fig. 1(d).

We also calculated the minority spin alignment, both spin- and orbital-resolved, for the V_2O_3/WSe_2 vdW heterostructure, as well as the atomic-resolved projected band structure using GGA+U. These results are respectively depicted in Fig. S4 and S5.

Next, we explored the effect of external electric fields on the electronic band structure in positive and negative directions. Interestingly, the direct band gap nature is preserved with an increase in the electric field, irrespective of the electric field direction. Our results are given in Table 1 for positive and negative directions.

As we know, among different 2D materials, some transition metal dichalcogenides (TMDs), including WS_2, WSe_2, $MoSe_2$ and MoS_2, are important for investigating valleytronics properties due to a peculiar characteristic of broken and preserved inversion symmetry in odd and even numbered layers, respectively.[15,28,56,57] In the present work, the main issue is to explore the valley polarization. As we discussed earlier, during heterostructure formation, we found an appreciable compressive strain of −2.89% in the WSe_2 monolayer; therefore, the question arises as to whether the current valley splitting originates from the strain effect or from the magnetic proximity effect induced due to the V_2O_3 monolayer. To address this issue, first, we calculate the effect of biaxial compressive strain (−2.89%) on the valley splitting of an isolated WSe_2 monolayer. The results are shown in the Fig. S6. Although this strain only reduces the electronic band gap, with a change from direct to indirect band gap. Furthermore, we found no lifting of the valley degeneracy. Thus, we conclude that the magnetic proximity effect induced by the magnetic V_2O_3 monolayer is responsible for valley splitting, as discussed in detail below.

Next, we need to achieve this goal of valley splitting, which is mainly due to the magnetic proximity effect induced by the V_2O_3 substrate. For this purpose, first, it is essential to understand valley splitting in terms of the twofold valley degree of freedom, as shown in Fig. 2(a) and (b). As shown in Fig. 2(a), in the presence of broken inversion symmetry and strong spin–orbit coupling, the interband optical transitions follow valley-dependent optical selection rules, allowing σ^+ (σ^-) circularly polarized optical transitions at K^+ and K^-.[58,59] Consequently,

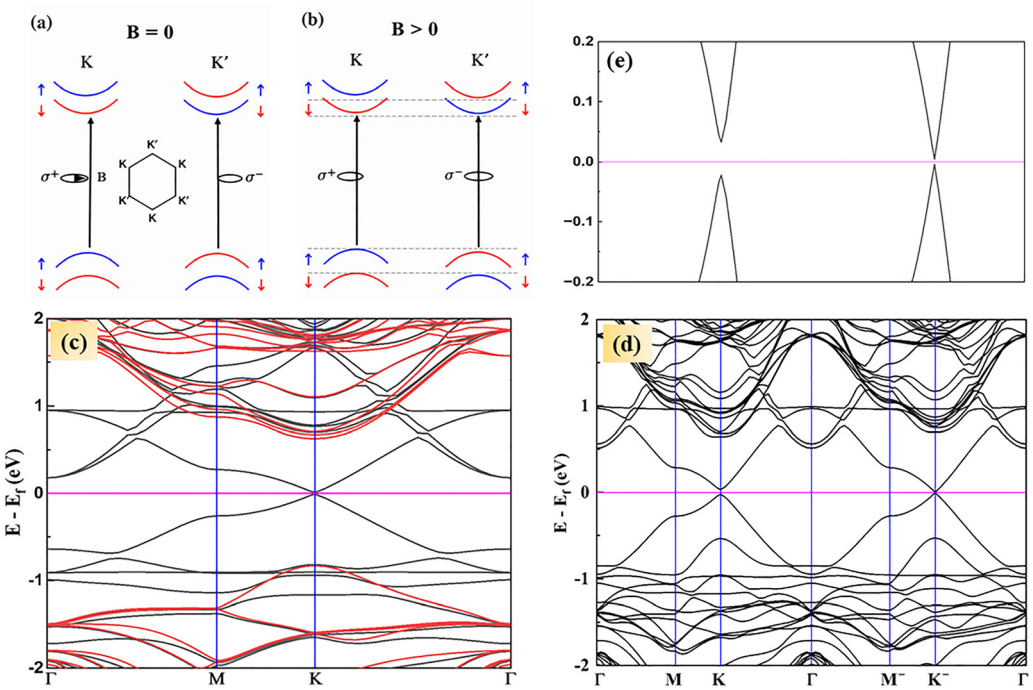

Fig. 2 Schematic of the band structures for the valley-dependent optical selection rule in the (a) WSe_2 ML and (b) V_2O_3/WSe_2 vdW heterostructure at K^+ and K^- due to the magnetic proximity effect, with B showing the induced magnetic field due to the V_2O_3 ML. PBE+U and SOC calculated band structures of the V_2O_3/WSe_2 vdW heterostructure at (c) K^+ and (d) K^-. (e) Magnified view of the band structure highlighting the band gaps at the K and K^- valleys.

the two valleys exhibit equivalent optical transition energies for circularly polarized light with an equivalent energy ($E_{\sigma^+} = E_{\sigma^-}$). Furthermore, at the conduction band maximum (CBM), the bands at K (C1, C2) and K′ (C′1, C′2) are very close to each other with an energy difference of 34 meV. Similarly, for VBM, these band states at K (V1, V2) and K′ (V′1, V′2) are slightly far away with an energy difference of 467 meV, as given in the Fig. S7.

Thus, this phenomenon results in equivalent energy for circularly polarized light ($E_{\sigma^+} = E_{\sigma^-}$), as shown in Fig. 2(a). Further, the SOC calculated band structure of the WSe_2 monolayer is also presented in Fig. S7, where both valleys at K^+ and K^-, with circularly polarized light, have an equivalent energy ($E_{\sigma^+} = E_{\sigma^-}$). Here, the energy difference between the two valleys at K^+ and K^- ($\Delta_1\uparrow - \Delta_2\uparrow$) is zero. While in the case of an external magnetic field B, not only is the inversion symmetry broken, but the time reversal symmetry also breaks down and thus their energies will no longer remain equivalent ($E_{\sigma^+} = E_{\sigma^-}$), as shown in Fig. 2(b) and thus the spins and valley can be distinguished. Similarly, in case of the V_2O_3/WSe_2 heterostructure, the magnetic proximity effect produced by the ferromagnetic V_2O_3 monolayer causes the valleys to behave as if they were in the presence of an external magnetic field, B. Therefore, the energy corresponding to the σ^+ circularly polarized light is 0.0104 eV at K^+, while for σ^-, it is −0.00015 eV at K^-, as shown in Fig. 2(d). Furthermore, Fig. 2(d) reveals that band-edge states associated with the valley degree of freedom are located at K and K^- with a finite energy difference at K^+ and K^- ($\Delta_1\uparrow - \Delta_2\uparrow$) of 10.41 meV, which confirms valley splitting due to broken inversion and time reversal symmetries. Interestingly, from these calculations, we confirm that the substrate ferromagnetic material (V_2O_3 ML) induces valley splitting like the magnetic proximity effect by the external magnetic field B.

To estimate the required external magnetic field B, we can use the k.p model,[60] where the interaction energy is given by the following equation:

$$H_B = g_0\mu_B B\cdot S + \mu_B B\cdot L, \quad (3)$$

where B shows the external magnetic field, g_0 is the Landé factor having a value of 2, μ_B is the Bohr magneton and $\mu_B = eh/2m_0$ with m_0 represents the mass of the electron. S and L respectively depict the spin and orbital angular momentum operators.

Next, to evaluate the applicability of the k.p model to our current system of the V_2O_3/WSe_2 vdW heterostructure, we further investigated the SOC-PROCAR results at the band edges. The orbital-resolved calculations reveal that both the CBM and VBM remain predominantly derived from the W-d orbitals, while the contribution from the V-d orbitals is negligible. However, compared with pristine WSe_2, the orbital contribution is partially modified due to the interfacial hybridization and electronic-state reconstruction. Therefore, the orbital characteristics obtained from pristine WSe_2 cannot be directly used to assign the exact orbital angular momentum quantum numbers associated with the band-edge states. Consequently, the conventional orbital angular momentum values of pristine WSe_2 ($L_z = 0$ for CBM) and ($L_z = 2$ for VBM), as shown in Fig. S7, can only provide an approximate description of the electronic states in the V_2O_3/WSe_2 vdW heterostructure. Therefore, the estimated effective magnetic field of 38.61 T corresponding to the valley splitting of 10.41 meV should be regarded as a qualitative measure of the

magnetic proximity effect rather than a quantitatively accurate value. Nevertheless, the sizeable valley splitting directly obtained from the first-principles calculations confirms the presence of strong exchange-induced valley polarization in the V_2O_3/WSe_2 vdW heterostructure.

Next, we applied an external electric field in the positive and negative directions and explored valley splitting. Interestingly, we found greater enhancement in valley splitting in the positive direction as compared to that in the negative direction. The results of valley splitting are given in Table 1 for both positive and negative electric field directions. From Table 1, the negative electric field first weakens the valley splitting and then enhances it due to charge redistribution and an increased strength of spin–orbit interactions. Therefore, overall, we found a competition between the charge redistribution and interfacial exchange coupling under the external electric field.

To further understand the interfacial interaction of the most stable configuration S1, we calculate and investigate the charge redistribution at the interface of the V_2O_3/WSe_2 heterostructure by using the relation:

$$\Delta_\rho = \rho_{\mathrm{Het}} - \rho_{\mathrm{WSe_2}} - \rho_{\mathrm{V_2O_3}} \quad (4)$$

where ρ_{Het}, $\rho_{\mathrm{WSe_2}}$, and $\rho_{\mathrm{V_2O_3}}$ are respectively the charge density of the vdW V_2O_3/WSe_2 vdW heterostructure, WSe_2 and V_2O_3 monolayers. The calculated charge density difference, as denoted by Δ_ρ, reveals a noticeable charge redistribution at the interface of the two monolayers for the electron depletion and accumulation, as depicted in Fig. 3. The yellow and cyan colors represent charge accumulation and depletion. To further confirm the transfer of charges from one layer to the other, we also performed a Bader charge analysis.[61,62] The negative and positive values represent the transfer of charge from V_2O_3 to WSe_2 monolayers or *vice versa*, respectively. A charge of 0.5924 e is lost by the W atoms of the WSe_2 monolayer, while the V and O atoms respectively gain a charge of 0.298 and 1.140 e. Further, the Se atoms towards the V_2O_3 monolayer also gain a charge of 0.245 e, while the Se atoms on the opposite side have an almost negligible contribution to the charge redistribution, as shown in Fig. 3. Interestingly, Fig. 3(a) also reveals the presence of an intrinsic built-in electric field originating from interfacial charge transfer between the V_2O_3 and WSe_2 monolayers. This charge redistribution leads to an asymmetric electrostatic potential across the interface, confirming strong interlayer coupling in the heterostructure. Consequently, a magnetic proximity effect emerges at the interface, where the magnetic ordering of the V_2O_3 monolayer induces a finite magnetic polarization in the adjacent WSe_2 layer. Notably, this induced magnetization is primarily localized on the Se atoms facing the V_2O_3 monolayer, while the Se atoms on the opposite side exhibit negligible magnetic moments due to the weak interaction with the ferromagnetic V_2O_3 monolayer. Further, this charge redistribution also modifies the electronic and magnetic properties of the V_2O_3/WSe_2 heterostructure.

Later, we also applied an external perpendicular electric field and explored the effect of the electric field on the charge density difference, as shown in Fig. 3(b) and (c), respectively, for ± 0.6 V Å^{-1}. Similarly, we also studied the effect of the electric field on the Bader charge analysis, as given in Table 2.

Interestingly, the Bader charge transfer has been confirmed from the charge density difference not only at zero electric field but also at a high electric field.

D. Magnetic properties

To study the effect of electric fields, first, we need to investigate the magnetic ground state of the pristine system. In the vdW V_2O_3/WSe_2 heterostructure, we consider both the ferromagnetic (FM) and the Néel anti-ferromagnetic (AFM) configurations, as shown in Fig. 1(a), by the blue arrows. For the FM and AFM spin configuration, we consider a unit cell of the V_2O_3/WSe_2 heterostructure. Where V atoms mainly contributed to the total magnetic moment, while other atoms have a negligible contribution to the total magnetic moment. According to Hund's rule, each electron in the V atom occupies the t_{2g} triplet state, which results in a 2 μ_B magnetic moment. In the case of AFM, one V atom has a magnetic moment of +2 while the other has -2 μ_B. Therefore, the total magnetic moment of the V_2O_3/WSe_2 vdW heterostructure is zero. Further, in the case of FM, each V

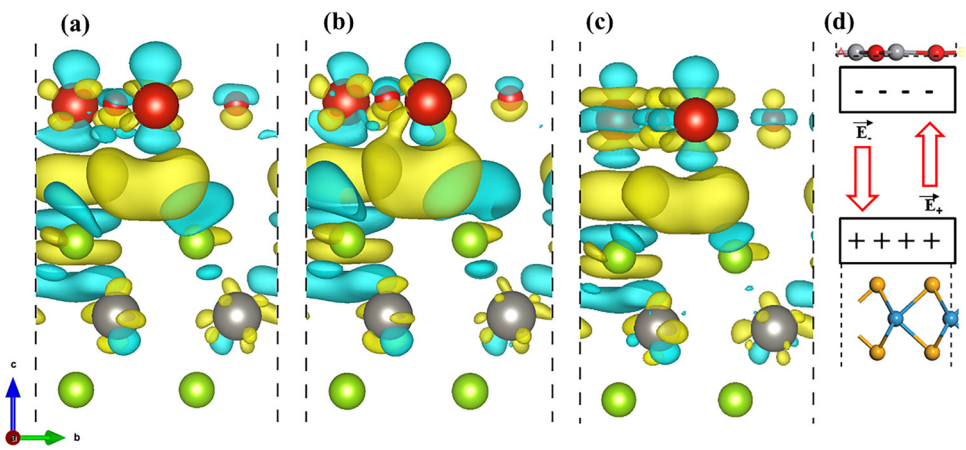

Fig. 3 Charge density difference of the V_2O_3/WSe_2 vdW heterostructure of the (a) pristine, (b) +0.6 and (c) -0.6 V Å^{-1} electric field. The cyan and yellow colors show the charge depletion and accumulation, respectively, with an iso-surface value of ± 0.0003 e Å^{-3}. (d) Direction of the electric field.

Table 2 Transfer of charges at different electric fields from WSe_2 (positive) to the V_2O_3 monolayer and *vice versa* (negative). The plus and minus values for charge transfer show the charge accumulation and depletion, respectively

	Positive				Negative			
	W	Se	V	O	W	Se	V	O
0.1	1.775	−0.932	0.052	−1.339	0.536	−0.303	−0.314	−1.115
0.2	1.768	−0.923	0.049	−1.344	0.686	−0.276	−0.327	−1.105
0.3	1.778	−0.929	0.048	−1.347	0.688	−0.267	−0.297	−1.122
0.4	1.775	−0.932	0.043	−1.350	0.596	−0.227	−0.271	−1.096
0.5	1.781	−0.941	0.042	−1.351	0.671	−0.298	−0.312	−1.105
0.6	1.777	−0.943	0.040	−1.354	0.662	−0.283	−0.284	−1.084

atom has a magnetic moment of 2 μ_B. Therefore, the total magnetic moment is 4 μ_B. Further, consistent with the Goodenough–Kanamori–Anderson (GKA) superexchange mechanism,[63–65] the magnetic moments mainly originate from the V atoms ~1.971, while small, induced moments of −0.14, 0.16 and 0.011 μ_B appear on neighboring O, W, and interfacial Se atoms due to hybridization. A 0.005 μ_B magnetic moment is also induced on Se atoms opposite to the V_2O_3 monolayer. The difference in energies between the anti-ferromagnetic (AFM) and ferromagnetic (FM) configuration states can be evaluated by using the following relation:

$$E_0 = E_{AFM} - E_{FM}, \quad (5)$$

where E_0, E_{AFM} and E_{FM}, respectively, stand for the energy of the current, anti-ferromagnetic and ferromagnetic ground states of the V_2O_3/WSe_2 vdW heterostructure. Remarkably, Table 1 also depicts that an increase in the external electric field from/to WSe_2 to the V_2O_3 monolayer does not robustly affect the ferromagnetic ground state of the V_2O_3/WSe_2 vdW heterostructure.

Later, we also calculated the magneto-crystalline anisotropy energy (MAE) by calculating non-collinear energies, including the spin–orbit (SOC) interaction along the in-plane [100] and out-of-plane [001] directions, which are called in-plane and out-of-plane directions. After applying SOC, the investigation of MAE can be conducted from the following expression:

$$\mathrm{MAE} = \xi^2 \sum_{u,o;\alpha,\beta} (2\delta_{\alpha\beta} - 1) \left[\frac{|\langle u,\alpha|\hat{L}z|o,\beta\rangle|^2 - |\langle u,\alpha|\hat{L}x|o,\beta\rangle|^2}{\varepsilon_{u,\alpha} - \varepsilon_{o,\beta}} \right], \quad (6)$$

where ξ shows the SOC coupling, while $\varepsilon_{u,\alpha}$ and $\varepsilon_{o,\beta}$ stand for unoccupied and occupied state energy levels, both in the spin-up (α) and down (β) orientations. Moreover, while the magnetic moment is largely governed only by the spin population difference and is thus insensitive to the orbital character, the MAE is strongly sensitive to the orbital character due to the SOC mechanism. Interestingly, we noted a giant MAE in the pristine

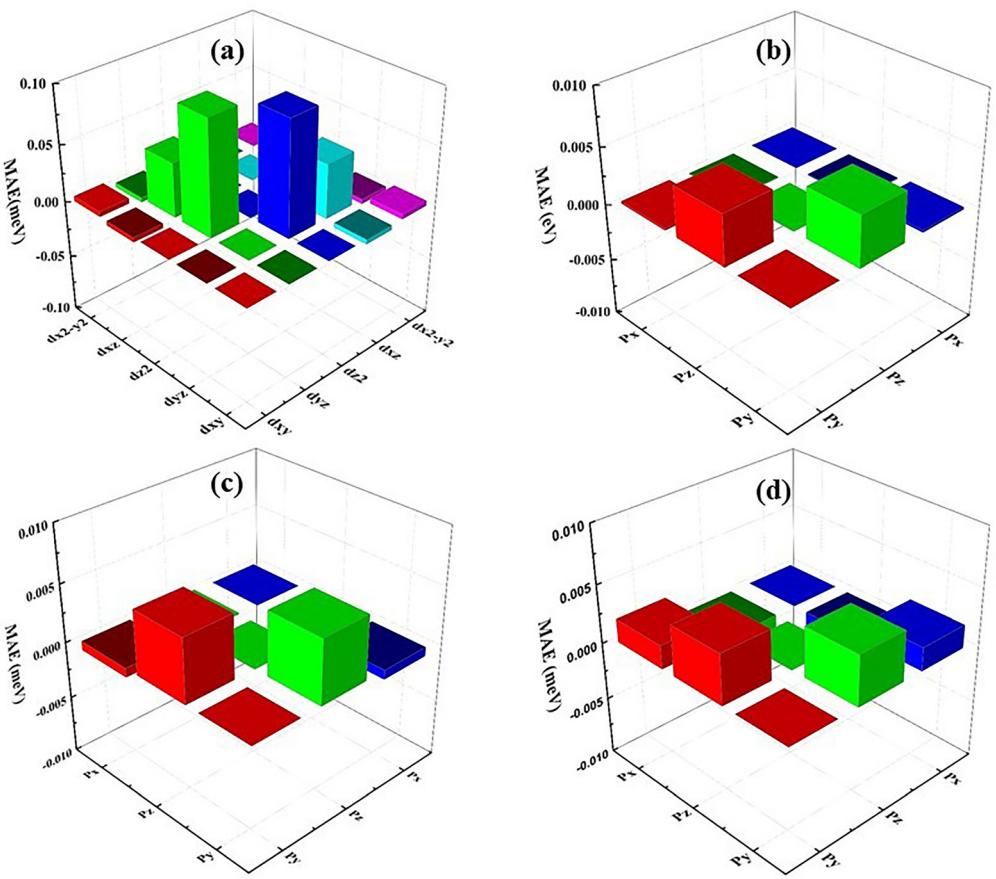

Fig. 4 SOC resolved MAE in the pristine V_2O_3/WSe_2 vdW heterostructure of (a) V, (b) O, (c) W and (d) Se.

V_2O_3/WSe_2 heterostructure. Further, the MAE of the V_2O_3/WSe_2 heterostructure increases with an increase in the positive electric field, while it decreases with an increase in the electric field in the opposite direction, as shown in Table 1. We also investigated the orbital-resolved contribution to the total MAE and found that in pristine V_2O_3/WSe_2 vdW heterostructure, only the V_d orbital contributes to the total magnetic anisotropy with an average value of 0.282 meV per V atom, while the contribution of other atoms is almost negligible, as shown in Fig. 4(b). Interestingly, the dominant contribution to the perpendicular MAE originates from the coupling between d_{yz} and d_{z^2}, while the next largest contribution arises from the interaction between d_{yz} and d_{xz} orbitals. Furthermore, Fig. 4(a) confirms that the d_{xy} and d_{xz} orbitals contribute negligibly to the total MAE. Similarly, for the other constituent atoms (O, W, and Se), we examined their orbital-resolved contribution to the total MAE. The results show that these three atoms contribute negligibly to the total MAE, with a marginally contribution from the W atom. However, in the case of the Se atom, the (p_z, p_y) orbital coupling favors the out-of-plane MAE, whereas the (p_x, p_y) orbital pair coupling of the O atoms contributes more significantly to the out-of-plane MAE, as shown in Fig. 4(b). It is important to note that we only investigate the atoms with a comparatively large contribution to MAE, which occupy the sites encircled as blue, black, red, and green dashed circles in Fig. 1(a), respectively, for V, O, W and Se atoms in the crystal structure of the V_2O_3/WSe_2 heterostructure. Furthermore, the external electric field does not affect the orbital-resolved contribution to the total MAE other than at the atomic sites, as shown in the Fig. S8.

Due to the electronegativity difference between the two monolayers forming the V_2O_3/WSe_2 heterostructure, an induced dipole moment is expected at the interface. To understand the origin of the charge transfer, we need to analyze the planar-average electrostatic potential and consequently the induced dipole moment, as shown in Fig. 5. The planar-average electrostatic potential is calculated along the *z*-axis, which is in accordance with the in-built or intrinsic electric field, as shown in Fig. 5(a). Furthermore, this in-built electric field causes a charge transfer from V_2O_3 to the WSe_2 ML even at zero electric field. Moreover, the planar electrostatic potential also confirms the orientation of both MLs, as shown in Fig. 5(a). Besides, both inversion and time-reversal symmetries are broken by the V_2O_3 ferromagnetic ML, and thus valley splitting occurs due to the magnetic proximity effect induced by the V_2O_3 ML. Interestingly, the in-plane magnetic proximity effect or effective magnetic field has no contribution to valley splitting, while the perpendicular effective magnetic field has a negligible effect on valley splitting.

The difference in electronegativity between the two layers not only results in an induced dipole moment but also a charge density difference. In the current calculations, we calculate the dipole moment along the *z*-direction, perpendicular to the

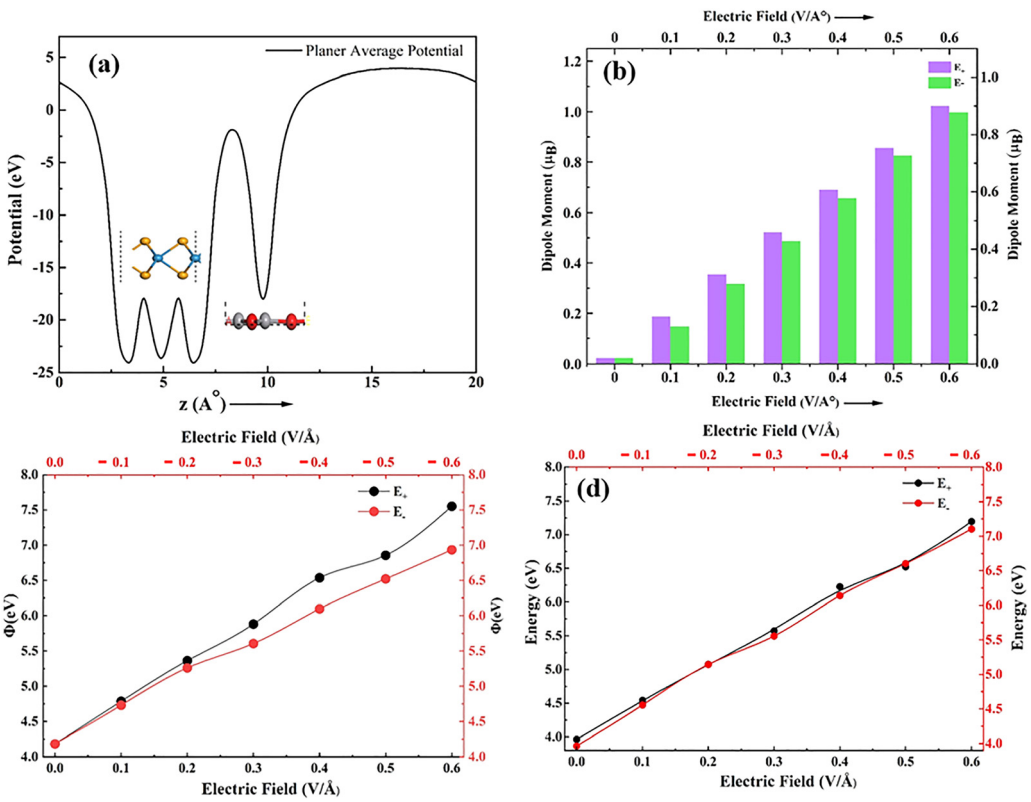

Fig. 5 (a) Electrostatic potential of the pristine V_2O_3/WSe_2 vdW heterostructure. Electric field-dependent (b) dipole moment, (c) work function (Φ) and (d) vacuum energy (F_V) of the V_2O_3/WSe_2 vdW heterostructure.

V_2O_3/WSe_2 vdW heterostructure using the following equation:

$$D_M = -\int \rho(z) z \mathrm{d}z + \sum N_i e z_i \quad (7)$$

In the above equation, $\rho(z)$ represents the valence electron density, z is the coordinate, N_i shows the atomic number of each ion i, and e is the charge of one proton. The charge redistribution at the interface of the heterostructure resulted in an induced dipole moment of 0.023 e Å. Interestingly, as the external perpendicular electric field increases either in the positive or negative direction, the dipole moment also increases, as shown in Fig. 5(b). This is due to the external perpendicular electric field and the internal in-built electric field, which is mainly due to the difference in electronegativity between the two layers of the V_2O_3/WSe_2 vdW heterostructure. Further, the enhancement in the dipole moment with increasing positive electric field is due to the greater inclination of the electronic charge from WSe_2 towards the V_2O_3 monolayer. Similarly, in the opposite direction, the dipole moment is still enhanced but with a negative sign only. A small difference in the dipole moment is only due to the built-in electric field because at zero electric field a dipole moment was induced between WSe_2 and V_2O_3 and more towards the V_2O_3 monolayer; it means an intrinsic electric field is induced due to the V_2O_3 ferromagnetic monolayer.

Similarly, to calculate the work function (Φ), we use the following relation:

$$\Phi = E_v - E_F, \quad (8)$$

where E_v is the vacuum energy extracted from the electrostatic potential profile along the z direction and E_F is the Fermi energy of the V_2O_3/WSe_2 vdW heterostructure. Due to the asymmetry in dipole moment in the V_2O_3/WSe_2 vdW heterostructure, the work function exhibits a stronger increase in the positive electric field direction than in the negative direction. Consequently, a significant potential difference is established across the V_2O_3/WSe_2 vdW heterostructure, providing further evidence for the existence of a built-in electric field, as shown in Fig. 5(c). We also found a significant difference in the vacuum energy (F_v) between positive and negative electric fields, as depicted in Fig. 5(d). Further, from eqn (6), at zero electric field, the charges will transfer to a layer with a high work function. It is clear from Table 2 that the charge transfer is greater due to the large value of the work function of WSe_2, while it goes down due to the negative electric field.

E. Curie temperature

Next, we also calculated the Curie Temperature of the V_2O_3/WSe_2 vdW heterostructure using the Metropolis Monte Carlo (MC) approach among the different available approaches. For this purpose, we use the VAMPIRE simulation package.[66] Here, we measured the temperature-dependent magnetization curve by using the Metropolis Monte Carlo (MC) simulation technique, which is implemented in the VAMPIRE software package and then extracted the Curie temperature (T_C). Further, the following classical spin Heisenberg model can be used as written below:

$$H = -\sum_{i,j} J m_i . m_j \quad (9)$$

In the above equation, J shows the energy parameter for exchange coupling of the first nearest-neighbor atom and m_i, m_j depict the magnetic moments of the nearest-neighbor atoms. Later, the $J_i = \frac{\Delta E}{Nm^2}$ can be used for calculating the exchange coupling energy parameter, where N shows the number of magnetic atoms in a unit cell and m represents the magnetic moment of each magnetic atom in the V_2O_3/WSe_2 vdW heterostructure unit cell.

Now, to run the Monte Carlo simulation code, we need a large enough supercell of $50 \times 50 \times 1$ so as to minimize finite-size effects and obtain long-range magnetic correlations and accurate thermodynamic properties like the Curie temperature. Further, the magnetization curve can be fitted by using the Curie–Bloch relation as given below:

$$m(T) = \left[1 - \frac{T}{T_C}\right]^{\beta}. \quad (10)$$

In the above equation, β is the critical exponent, with different values used for fitting the temperature-dependent magnetization curve, as shown in Fig. 6. Here, the value for this critical exponent is 0.49.

This Figure shows that initially, the magnetization curve retains its high values due to the high spin state in the low temperature range due to its stable ferromagnetic ordering and gradually decreases with an increase in temperature, and eventually, it drops to zero near the critical temperature. From these Monte Carlo simulations, we obtained a Curie temperature of approximately 500 K for the pristine V_2O_3/WSe_2 vdW heterostructure. To verify the implementation of the Heisenberg Monte Carlo methodology, we also estimated the Curie temperature of the CrI_3 monolayer and found it to be 46 K, which agrees well with the experimentally reported value of 45 K.[67] It is worth mentioning that our intention of this comparison is solely as a methodological benchmark of the Monte Carlo implementation and should not be regarded as a universal validation of the Monte Carlo simulation approach for all ferromagnetic oxide materials. Further, this comparison shows good agreement between the experimental and theoretical Curie temperatures of CrI_3, which shows that the current adopted simulation framework can reasonably capture the magnetic phase transition behavior in well-established two-dimensional magnetic materials.

Furthermore, we also compared our results with the Mean Field Theory (MFT) approach and found that the MFT results are overestimated. Later, we also calculated the Curie temperature at a high external electric field, as shown in Fig. 6(b) and (c) for 0.6 V $Å^{-1}$ both in the positive and negative directions. Interestingly, we found that the Curie temperatures at +0.6 and −0.6 V $Å^{-1}$ are 530 and 710 K, respectively. We also calculated the Curie temperature at all remaining steps as

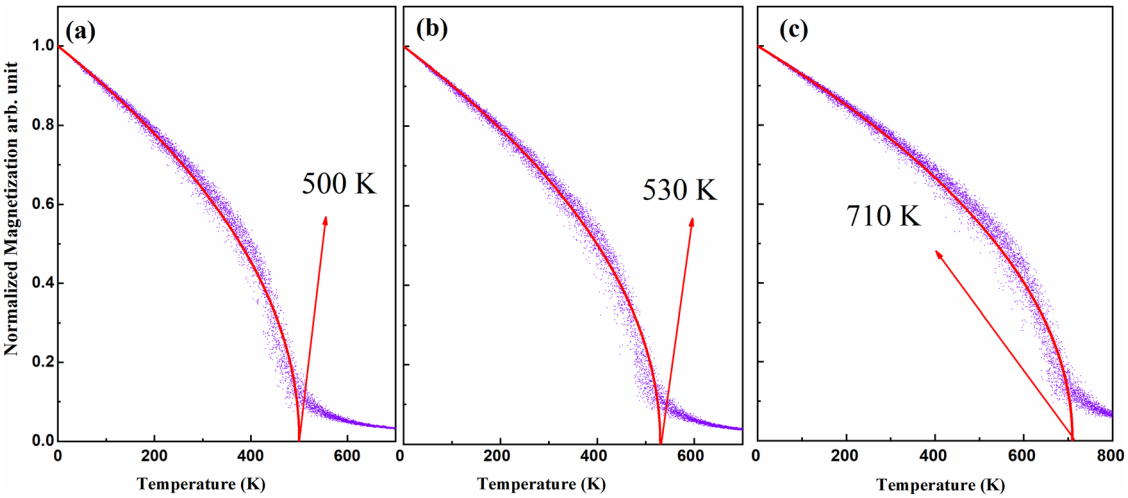

Fig. 6 Curie temperature of the V_2O_3/WSe_2 heterostructure at the pristine state (a), +0.6 V Å^{-1} (b) and −0.6 V Å^{-1} (c). The purple dotted curve shows the temperature-dependent magnetization curve, while the red line shows the fitted result with eqn (9).

given in the Table S1. Similarly, information about the magnetic moment and exchange energy is also listed in Table S1.

IV. Discussion

In the current study, besides the structural, electronic, and magnetic properties, we also explored the valleytronics properties of the V_2O_3/WSe_2 vdW heterostructure. The V_2O_3/WSe_2 vdW heterostructure had a direct band gap of 0.02 eV. Applying spin–orbit interactions, the magnetic proximity effect causes a giant valley splitting of 10.41 meV in the V_2O_3/WSe_2 vdW heterostructure. Similarly, non-collinear total energy calculations confirm an out-of-plane magnetocrystalline anisotropy with a prominent value of 0.31 meV. Further, using Metropolis Monte Carlo (MC) simulations, we found a Curie temperature of 500 K for the pristine V_2O_3/WSe_2 vdW heterostructure. We applied an external electric field in the perpendicular direction to the V_2O_3/WSe_2 vdW heterostructure and explored the effect of the electric field on the structural, electronic, and magnetic properties of the V_2O_3/WSe_2 vdW heterostructure. Interestingly, we found that ferromagnetism remains preserved irrespective of the electric field direction. Further, an abrupt enhancement in valley splitting of the V_2O_3/WSe_2 vdW heterostructure has also been found. The Bader charge analysis confirmed charge transfer from/to V_2O_3 to/from WSe_2 monolayers. This charge transfer induces an in-built electric field at the interface, which can either enhance or weaken the effect of the external electric field applied in the parallel/opposite directions. Consequently, the superexchange interaction described by the Goodenough–Kanamori–Anderson rule is further strengthened, leading to the induction or modification of magnetic moments of the constituent atoms in the V_2O_3/WSe_2 vdW heterostructure. This phenomenon is commonly referred to as the magnetic proximity effect. Therefore, the applied external electric field plays a decisive role in controlling the electronic, magnetic, and structural properties of the V_2O_3/WSe_2 vdW heterostructure. Therefore, our studies suggest that an external electric field is a promising technique to control spin and valleytronics applications in oxide-based vdW heterostructures.

Author contributions:

J. J. and G. Q. supervised the project. F. S. conceived the idea, performed the DFT calculations, and plotted the results. All the authors carefully checked the results and helped with writing and editing the manuscript.

Conflicts of interest

The authors have no conflicts of interest.

Data availability

Data will be made available upon request.

The supplementary information (SI) contains the following informations optimized WSe_2 structure, stacking configurations, interlayer distance, spin-orbital and atom-resolved band structures, strained and pristine SOC band structures, MAE under different electric fields, magnetic moment, exchange coupling and Curie temperature at different electric fields are given in the supplementary information. See DOI: https://doi.org/10.1039/d6tc01261b.

Acknowledgements

This work was supported by the Industrial Technology Innovation Program (RS-2024-00435432: Development of hydrogen production technology through ammonia decomposition using a plasmonics-based light system with high performance and long-term durability), funded by the Ministry of Trade, Industry & Energy (MOTIE, Korea). This research was supported by the Brain Pool program funded by the Ministry of Science and ICT through the National Research Foundation of Korea (RS-2025-25396197). G. Q. was supported by the National Key R&D

Program of China (2023YFB2408100), the Fundamental Research Funds for the Central Universities (Grant No. 531119200237), the Guangdong Basic and Applied Basic Research Foundation (2025A1515012237), the State Key Laboratory of Robotics and Systems at the Harbin Institute of Technology (SKLRS-2025-KF-10), the National Major Science and Technology Project of China (Grant No. 2025ZD0717301), and the Open Project of the Shaanxi Key Laboratory of Gear Transmission (Grant No. SKLGT-2024-005).

References

1 B. Huang, G. Clark, E. Navarro-Moratalla, D. R. Klein, R. Cheng, K. L. Seyler, D. Zhong, E. Schmidgall, M. A. McGuire, D. H. Cobden, W. Yao, D. Xiao, P. Jarillo-Herrero and X. Xu, *Nature*, 2017, **546**, 270–273.
2 S. Tian, J.-F. Zhang, C. Li, T. Ying, S. Li, X. Zhang, K. Liu and H. Lei, *J. Am. Chem. Soc.*, 2019, **141**, 5326–5333.
3 C. Gong, L. Li, Z. Li, H. Ji, A. Stern, Y. Xia, T. Cao, W. Bao, C. Wang, Y. Wang, Z. Q. Qiu, R. J. Cava, S. G. Louie, J. Xia and X. Zhang, *Nature*, 2017, **546**, 265–269.
4 Y. Deng, Y. Yu, Y. Song, J. Zhang, N. Z. Wang, Z. Sun, Y. Yi, Y. Z. Wu, S. Wu, J. Zhu, J. Wang, X. H. Chen and Y. Zhang, *Nature*, 2018, **563**, 94–99.
5 V. L. Korenev, I. A. Akimov, S. V. Zaitsev, V. F. Sapega, L. Langer, D. R. Yakovlev, Y. A. Danilov and M. Bayer, *Nat. Commun.*, 2012, **3**, 959.
6 B. Scharf, G. Xu, A. Matos-Abiague and I. Žutić, *Phys. Rev. Lett.*, 2017, **119**, 127403.
7 C. Lee, F. Katmis, P. Jarillo-Herrero, J. S. Moodera and N. Gedik, *Nat. Commun.*, 2016, **7**, 12014.
8 J. Stahn, J. Chakhalian, Ch Niedermayer, J. Hoppler, T. Gutberlet, J. Voigt, F. Treubel, H.-U. Habermeier, G. Cristiani, B. Keimer and C. Bernhard, *Phys. Rev. B: Condens. Matter Mater. Phys.*, 2005, **71**, 140509.
9 A. K. Geim and I. V. Grigorieva, *Nature*, 2013, **499**, 419–425.
10 Y. Wu, J. Tong, L. Deng, F. Luo, F. Tian, G. Qin and X. Zhang, *Nano Lett.*, 2023, **23**, 6226–6232.
11 V. L. Berezinsky, *Sov. Phys. JETP*, 1971, **32**, 493–500.
12 J. M. Kosterlitz and D. J. Thouless, *J. Phys. C: Solid State Phys.*, 1973, **6**, 1181.
13 N. D. Mermin and H. Wagner, *Phys. Rev. Lett.*, 1966, **17**, 1133–1136.
14 L. Onsager, *Phys. Rev.*, 1944, **65**, 117–149.
15 J. Yu, X. Kuang, J. Zhong, L. Cao, C. Zeng, J. Ding, C. Cong, S. Wang, P. Dai, X. Yue, Z. Liu and Y. Liu, *Opt. Exp.*, 2020, **28**, 13260–13268.
16 A. F. Young, C. R. Dean, L. Wang, H. Ren, P. Cadden-Zimansky, K. Watanabe, T. Taniguchi, J. Hone, K. L. Shepard and P. Kim, *Nat. Phys.*, 2012, **8**, 550–556.
17 D. Xiao, W. Yao and Q. Niu, *Phys. Rev. Lett.*, 2007, **99**, 236809.
18 W. Yao, D. Xiao and Q. Niu, *Phys. Rev. B:Condens. Matter Mater. Phys.*, 2008, **77**, 235406.
19 J. R. Schaibley, H. Yu, G. Clark, P. Rivera, J. S. Ross, K. L. Seyler, W. Yao and X. Xu, *Nat. Rev. Mater.*, 2016, **1**, 16055.
20 G. Aivazian, Z. Gong, A. M. Jones, R.-L. Chu, J. Yan, D. G. Mandrus, C. Zhang, D. Cobden, W. Yao and X. Xu, *Nat. Phys.*, 2015, **11**, 148–152.
21 F. Bussolotti, H. Kawai, Z. E. Ooi, V. Chellappan, D. Thian, A. L. C. Pang and K. E. J. Goh, *Nano Futures*, 2018, **2**, 032001.
22 J. Lee, K. F. Mak and J. Shan, *Nat. Nanotech.*, 2016, **11**, 421–425.
23 H. Zeng, J. Dai, W. Yao, D. Xiao and X. Cui, *Nat. Nanotech.*, 2012, **7**, 490–493.
24 E. J. Sie, J. W. McIver, Y.-H. Lee, L. Fu, J. Kong and N. Gedik, *Nat. Mater.*, 2015, **14**, 290–294.
25 K. F. Mak, K. L. McGill, J. Park and P. L. McEuen, *Science*, 2014, **344**, 1489–1492.
26 Z. Zhang, X. Ni, H. Huang, L. Hu and F. Liu, *Phys. Rev. B*, 2019, **99**, 115441.
27 K. Zollner, P. E. Faria Jr and J. Fabian, *Phys. Rev. B*, 2019, **100**, 085128.
28 D. MacNeill, C. Heikes, K. F. Mak, Z. Anderson, A. Kormányos, V. Zólyomi, J. Park and D. C. Ralph, *Phys. Rev. Lett.*, 2015, **114**, 037401.
29 G. Moody, K. Tran, X. Lu, T. Autry, J. M. Fraser, R. P. Mirin, L. Yang, X. Li and K. L. Silverman, *Phys. Rev. Lett.*, 2018, **121**, 057403.
30 A. Ramasubramaniam and D. Naveh, *Phys. Rev. B:Condens. Matter Mater. Phys.*, 2013, **87**, 195201.
31 Y. Zhu, T. Chen, Y. Li, L. Qiao, X. Ma, C. Liu, T. Hu, H. Gao and W. Ren, *Nano Lett.*, 2024, **24**, 472–478.
32 F. Yang, J. Shang, L. Kou, C. Li and Z. Deng, *Nanomaterials*, 2022, **12**, 2461.
33 Q. Tan, A. Rasmita, S. Li, S. Liu, Z. Huang, Q. Xiong, S. A. Yang, K. S. Novoselov and W. Gao, *Sci. Adv.*, 2021, **7**, eabh0863.
34 Y. Wu, L. Deng, X. Yin, J. Tong, F. Tian and X. Zhang, *Nano Lett.*, 2024, **24**, 10534–10539.
35 L. Deng, F. Wang, X. Yin, J. Tong, Y. Wu and X. Zhang, *J. Am. Chem. Soc.*, 2026, **148**, 1837–1846.
36 N. Tripathy and A. De Sarkar, *Appl. Phys. Lett.*, 2025, **126**, 232107.
37 B. Zhai, J. Du, C. Shen, T. Wang, Y. Peng, Q. Zhang and C. Xia, *Phys. Rev. B*, 2019, **100**, 195307.
38 K. L. Seyler, D. Zhong, B. Huang, X. Linpeng, N. P. Wilson, T. Taniguchi, K. Watanabe, W. Yao, D. Xiao, M. A. McGuire, K.-M. C. Fu and X. Xu, *Nano Lett.*, 2018, **18**, 3823–3828.
39 D. Zhong, K. L. Seyler, X. Linpeng, R. Cheng, N. Sivadas, B. Huang, E. Schmidgall, T. Taniguchi, K. Watanabe, M. A. McGuire, W. Yao, D. Xiao, K.-M. C. Fu and X. Xu, *Sci. Adv.*, 2017, e1603113.
40 T. Hu, G. Zhao, H. Gao, Y. Wu, J. Hong, A. Stroppa and W. Ren, *Phys. Rev. B*, 2020, **101**, 125401.
41 M. Ge, H. Wang, J. Wu, C. Si, J. Zhang and S. Zhang, *npj Comput Mater*, 2022, **8**, 1–7.
42 I. Khan, B. Marfoua and J. Hong, *npj 2D Mater. Appl.*, 2021, **5**, 1–8.
43 G. Kresse and D. Joubert, *Phys. Rev. B:Condens. Matter Mater. Phys.*, 1999, **59**, 1758–1775.
44 G. Kresse and J. Furthmüller, *Phys. Rev. B:Condens. Matter Mater. Phys.*, 1996, **54**, 11169–11186.

45 J. P. Perdew, K. Burke and M. Ernzerhof, *Phys. Rev. Lett.*, 1996, **77**, 3865–3868.
46 H. J. Monkhorst and J. D. Pack, *Phys. Rev. B*, 1976, **13**, 5188–5192.
47 S. Grimme, J. Antony, S. Ehrlich and H. Krieg, *J. Chem. Phys.*, 2010, **132**, 154104.
48 S. L. Dudarev, G. A. Botton, S. Y. Savrasov, C. J. Humphreys and A. P. Sutton, *Phys. Rev. B:Condens. Matter Mater. Phys.*, 1998, **57**, 1505–1509.
49 F. Subhan, C. Gao, L. Ali, Y. Zhou, Z. Qin and G. Qin, *J. Phys. Chem. C*, 2024, **128**, 9802–9811.
50 J. Rehman, R. Ali, N. Ahmad, X. Lv and C. Guo, *J. Alloys Compd.*, 2019, **804**, 370–375.
51 J.-K. Huang, J. Pu, C.-L. Hsu, M.-H. Chiu, Z.-Y. Juang, Y.-H. Chang, W.-H. Chang, Y. Iwasa, T. Takenobu and L.-J. Li, *ACS Nano*, 2014, **8**, 923–930.
52 C. Yang, X. Zhao and S. Wei, *Solid State Commun.*, 2016, **245**, 70–74.
53 K. Zollner, P. E. Faria Jr and J. Fabian, *Phys. Rev. B*, 2019, **100**, 085128.
54 K. S. Novoselov, A. Mishchenko, A. Carvalho and A. H. Castro Neto, *Science*, 2016, **353**, aac9439.
55 C. S. Boland, Y. Sun and D. G. Papageorgiou, *Nano Lett.*, 2024, **24**, 12722–12732.
56 Y. Liu, Y. Gao, S. Zhang, J. He, J. Yu and Z. Liu, *Nano Res.*, 2019, **12**, 2695–2711.
57 J. Yu, X. Kuang, Y. Gao, Y. Wang, K. Chen, Z. Ding, J. Liu, C. Cong, J. He, Z. Liu and Y. Liu, *Nano Lett.*, 2020, **20**, 1172–1182.
58 D. Xiao, G.-B. Liu, W. Feng, X. Xu and W. Yao, *Phys. Rev. Lett.*, 2012, **108**, 196802.
59 D. Zhong, K. L. Seyler, X. Linpeng, N. P. Wilson, T. Taniguchi, K. Watanabe, M. A. McGuire, K.-M. C. Fu, D. Xiao, W. Yao and X. Xu, *Nat. Nanotechnol.*, 2020, **15**, 187–191.
60 G. Wang, L. Bouet, M. M. Glazov, T. Amand, E. L. Ivchenko, E. Palleau, X. Marie and B. Urbaszek, *2D Mater.*, 2015, **2**, 034002.
61 G. Henkelman, A. Arnaldsson and H. Jónsson, *Comput. Mater. Sci.*, 2006, **36**, 354–360.
62 W. Tang, E. Sanville and G. Henkelman, *J. Phys.: Condens. Matter*, 2009, **21**, 084204.
63 J. B. Goodenough, *Phys. Rev.*, 1955, **100**, 564–573.
64 J. Kanamori, *J. Phys. Chem. Solids*, 1959, **10**, 87–98.
65 P. W. Anderson, *Phys. Rev.*, 1959, **115**, 2–13.
66 R. F. L. Evans, W. J. Fan, P. Chureemart, T. A. Ostler, M. O. A. Ellis and R. W. Chantrell, *J. Phys.: Condens. Matter*, 2014, **26**, 103202.
67 B. Huang, G. Clark, E. Navarro-Moratalla, D. R. Klein, R. Cheng, K. L. Seyler, D. Zhong, E. Schmidgall, M. A. McGuire, D. H. Cobden, W. Yao, D. Xiao, P. Jarillo-Herrero and X. Xu, *Nature*, 2017, **546**, 270–273.

